Results in Engineering 30 (2026) 110002

Contents lists available at ScienceDirect

Results in Engineering

journal homepage: www.sciencedirect.com/journal/results-in-engineering

Research paper

Predictive degradation modeling with optimized interconnectors for enhancing solid oxide electrolyzer cell durability in sustainable syngas production

Abrar Ahmad [a,b], Serene Sow Mun Lock [a,b,*], Lam Ghai Lim [c], Irene Sow Mei Lock [d], Grazia Leonzio [e], Chung Loong Yiin [f,g], Chrisminder Dain [h]

[a] Centre of Carbon Capture, Utilisation and Storage (CCCUS), Universiti Teknologi PETRONAS, Seri Iskandar 32610, Malaysia
[b] Department of Chemical Engineering, Universiti Teknologi PETRONAS, Seri Iskandar 32610, Malaysia
[c] Department of Electrical and Robotics Engineering, School of Engineering, Monash University Malaysia, Jalan Lagoon Selatan, Bandar Sunway 47500, Selangor, Malaysia
[d] Group Technical Solutions, Project Delivery and Technology Division, PETRONAS, Kuala Lumpur 50088, Malaysia
[e] Cagliari University, Department of Mechanical, Chemical and Materials Engineering, via Marengo 2, 09123 Cagliari, Italy
[f] Department of Chemical Engineering and Energy Sustainability, Faculty of Engineering, Universiti Malaysia Sarawak (UNIMAS), Kota Samarahan 94300, Sarawak, Malaysia
[g] Institute of Sustainable and Renewable Energy (ISuRE), Universiti Malaysia Sarawak (UNIMAS), Kota Samarahan 94300, Sarawak, Malaysia
[h] PETRONAS Research Sdn Bhd, 43000, Bandar Baru Bangi, Selangor Darul Ehsan, Malaysia

ARTICLE INFO

Keywords:
Solid oxide electrolyzer cell (SOEC)
Co-electrolysis
Syngas production
Structure degradation
Antioxidant layer
Modelling and simulation

ABSTRACT

Solid oxide electrolyzer cells offer a promising solution for sustainable syngas production via high-temperature co-electrolysis of water and CO_2. However, their long-term performance is limited by structural degradation, including cathode sintering, electrolyte phase transitions, anode delamination, and interconnector oxidation, which degrade electrochemical stability and efficiency. These degradation effects are often simplified in existing modeling studies. To address this, a material-specific degradation model was developed in Aspen Custom Modeler to simulate SOEC behavior under varying conditions. The model incorporated nickel sintering, yttria-stabilized zirconia phase changes, and interconnector oxidation. Simulation results revealed that interconnectors degrade faster, reducing the triple-phase boundary length, critical for electrochemical activity. Applying a lanthanum strontium cobaltite coating to interconnectors reduced degradation by 40.34 %, enhancing SOEC durability. These findings underscore the potential of predictive modeling combined with advanced coatings to improve SOEC performance for sustainable syngas production.

1.0. Introduction

Global energy and environmental concerns have increased due to rapid industrialization and population growth, leading to rise in greenhouse gas emissions, with carbon dioxide (CO_2) being a major contributor, reaching 37.8 Gt in 2024 (0.8 % above 2023), and atmospheric levels at 422.5 ppm [1–3]. This issue has consequently received widespread environmental and energy attention in recent years. Fossil fuel combustion remains the primary driver of global warming and energy imbalance, leading the Intergovernmental Panel on Climate Change (IPCC) to emphasize the need for net-zero emissions by 2050 [4–6]. This underscores the need to transition our focus towards renewable energy sources. In this direction, significant research efforts are already underway to advance CO_2 reduction and conversion technologies in parallel with clean alternatives such as solar and wind energy, aiming to meet energy demands while mitigating climate impacts [7]. Given these considerations, reducing CO_2 emissions and converting them into value-added products is a promising solution [8].

Among decarbonization pathways, electrochemical CO_2 conversion offers a viable pathway by transforming waste carbon into fuels and chemicals [9]. This method is highly attractive as it combines energy efficiency with cost-effectiveness by enabling hydrocarbon fuel production from CO_2, water, and renewable sources. It offers precise process control, compact and easily integrable design, high efficiency, modular

* Corresponding author at: Department of Chemical Engineering, Universiti Teknologi PETRONAS, Seri Iskandar 32610, Malaysia.
E-mail address: sowmun.lock@utp.edu.my (S.S.M. Lock).

https://doi.org/10.1016/j.rineng.2026.110002
Received 17 October 2025; Received in revised form 7 February 2026; Accepted 9 March 2026
Available online 10 March 2026

scalability, on-demand operation, and the flexibility to utilize diverse clean energy resources and surplus electricity [10,11]. Within this framework, solid oxide electrolyzer cells (SOECs) represent a particularly promising electrochemical process, as they operate at higher temperatures where both thermodynamic and kinetic conditions are highly favorable. This allows the simultaneous co-electrolysis of CO_2 and H_2O to produce syngas, a tailored mixture of carbon monoxide (CO) and hydrogen (H_2). Syngas is a critical intermediate that can be further upgraded into synthetic fuels, such as methanol, Fischer-Tropsch hydrocarbons, and ammonia, as well as other value-added chemicals [12–15]. However, their commercial adoption is hindered by long-term degradation of the cell operations, including Ni coarsening in fuel electrodes [16], interconnect oxidation [17], oxygen electrode delamination [18], and phase changes in the electrolyte [19], which limit efficiency and commercialization [10,20].

SOEC stacks consist of series-connected cells with dense electrolytes, fuel, and oxygen electrodes, linked by ferritic stainless-steel interconnects that ensure electrical continuity, gas separation, and stability. Interconnectors such as Crofer 22 APU and Haynes 230 are widely used due to their conductivity, thermal expansion compatibility, and cost-effectiveness [12,21–23]. However, at high operating temperatures (700–850 °C), chromium in these alloys reacts with oxygen to form a chromium oxide (Cr_2O_3) scale at the interconnect-anode interface. While this oxide layer initially provides protection, its continuous growth increases electrical resistance and reduces efficiency. Moreover, volatile chromium species can migrate to the oxygen electrode, where they block active sites, a process known as chromium poisoning, which further accelerates SOEC degradation [10,17,24,25]. Therefore, interconnect materials must combine high electrical/thermal conductivity, corrosion resistance, thermal expansion compatibility, and cost-effectiveness [26]. Metallic alloys, particularly ferritic stainless steels, are preferred over ceramics due to superior manufacturability, mechanical strength, cost-effectiveness, and higher conductivity [27–29]. Ferritic stainless steels such as AISI 430 [30], Crofer 22 APU [31,32], Crofer 22 H [33], E-Brite [34], Haynes 230 [35]. Among these, Crofer 22 APU offers optimal coefficient of thermal expansion (CTE) matching, high-temperature stability, low cost, and strong electrical performance [36–38].

To further enhance the durability of the interconnector, protective coatings have been explored. While Mn-Co spinel coatings are widely used for SOEC interconnect protection, their lower conductivity (~40–60 S cm^{-1}) and higher long-term area-specific resistance (ASR) can limit current collection efficiency [39,40]. Noble metals offer excellent conductivity but are costly and prone to migration during operation [25]. In contrast, perovskite coatings such as lanthanum strontium cobaltite ($La_{0.8}Sr_{0.2}CoO_3$, LSC) provide high conductivity (>200 S cm^{-1} at 800 °C), strong chemical stability, oxidation resistance, and effective suppression of chromium evaporation, making them attractive for SOEC interconnect protection [18,30,41–45].

Although previous studies have made efforts to model SOEC degradation, significant limitations persist, particularly in capturing the interactions among microstructural changes and degradation linked to interconnectors, such as chromium oxide scale formation, volatilization, and interactions with electrode surfaces, which remain insufficiently represented in most models, despite their critical influence on overall stack performance and durability. Kamkeng et al. [46] incorporated Ni coarsening and LSM-YSZ phase degradation into a COMSOL-based 2D co-electrolysis model, yet their work focused on short-term operation without coupling multiple degradation mechanisms. Similarly, Xia et al. [47] quantified performance loss due to LSM-YSZ phase coarsening using an experimental model hybrid approach, but interconnect oxidation and long-term effects were not considered. Yang et al. [48] investigated ferritic stainless-steel interconnect oxidation under accelerated testing, identifying Cr_2O_3 scale growth rates, though the study was limited to ≤ 3000 h and did not address breakaway corrosion. Luo et al. [49] analyzed electrolyte phase transitions through microstructural characterization, linking them to reduced ionic conductivity, but this was not integrated into stack-level co-electrolysis simulations. Wang et al. [50] developed a 3D multi-physics COMSOL model to simulate heat, mass, and charge transfer, yet assumed constant material properties without degradation coupling. Zhang et al. [13] demonstrated that LSC coatings could reduce oxide scale growth on interconnects, though voltage stability and syngas yield impacts were not evaluated.

Collectively, these studies highlight that while individual degradation phenomena have been investigated, comprehensive long-term modeling that couples structural, electrochemical, and interconnect-related degradation under co-electrolysis conditions remains lacking. Many simulations address pure H_2O or CO_2 electrolysis, leaving co-electrolysis durability underexplored [51–54]. Recent efforts have begun to incorporate structural degradation into co-electrolysis modeling, but remain limited in scope [47,55,56]. Degradation linked to LSM-YSZ phase coarsening affects long-term stack performance, and although interconnect oxidation has been studied over short durations, typically a few thousand hours, the longer-term effects, such as breakaway corrosion and oxide scale spallation, remain insufficiently addressed [10,24,25,48,57–60]. Structural degradations such as LSM-YSZ phase coarsening and long-term interconnect oxidation remain insufficiently modeled [14,21,61–63], with COMSOL-based 1D, 2D models often overlooking degradation in co-electrolysis [18,50,64,65]. Durability remains the key barrier to SOEC commercialization since progressive degradation directly impacts electrochemical performance by increasing resistive and kinetic overpotentials. Hypothetically, an integrated framework that couples all major degradation mechanisms over extended operating periods could enable more accurate lifetime prediction and guide the design of next-generation SOEC stacks with enhanced durability.

This study presents a validated electrochemical model for solid oxide electrolysis cells developed in Aspen Custom Modeler, integrating performance and degradation mechanisms under CO_2/H_2O co-electrolysis conditions. The physics-based framework enables long-term prediction of SOEC behavior and systematically evaluates the effects of operating parameters such as current density, temperature, gas composition, and flow rate on durability and syngas production efficiency. Multiple degradation mechanisms, including nickel particle sintering, electrolyte ionic conductivity degradation, electrode delamination, and chromium oxide scale growth at the interconnect, are incorporated within a unified simulation platform. In addition, the impact of lanthanum strontium cobaltite coatings on Crofer 22 APU interconnects in mitigating corrosion and oxidation-induced degradation is quantitatively assessed. Model predictions are validated against experimental data and extended to industrially relevant operating times, providing insight into durability-limiting mechanisms in SOEC co-electrolysis systems and demonstrating the potential of interconnect surface engineering to enhance long-term stability and support the design of high-efficiency syngas production systems.

2.0. Mathematical modelling

2.1. Cell description

The model SOEC is a planar, single-cell configuration designed to operate under H_2O/CO_2 co-electrolysis conditions, simulating long-term electrochemical performance and degradation behavior. A simple schematic description of the SOEC is presented in Fig. 1 (a). The cell comprises a Ni-YSZ fuel electrode (cathode), a dense YSZ electrolyte, an LSM-YSZ oxygen electrode (anode), and Crofer 22 APU ferritic stainless-steel interconnects [66]. The model, developed in ACM, breaks the cell into parts: cathode, electrolyte, anode, and interconnects. It helps study charge transfer, gas flow, and structural damage. This approach allows for a detailed analysis of each component's behavior. Electrochemical reactions occur primarily at the cathode, where CO_2 and H_2O are reduced to form CO and H_2, releasing oxygen ions (O^{2-}) that migrate

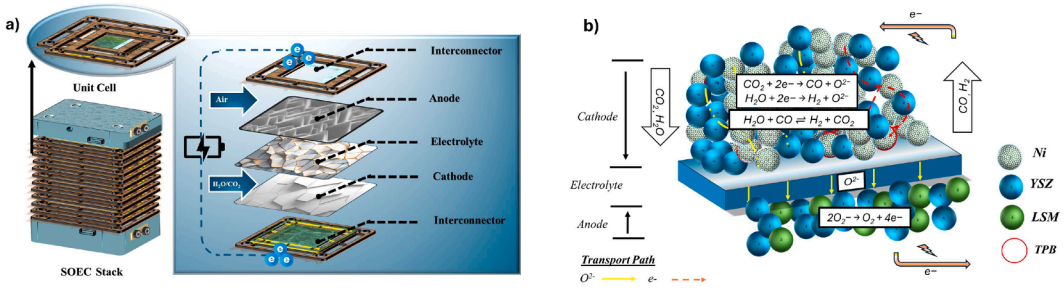

Fig. 1. Schematic of (a) SOEC Description and (b) SOEC Configuration.

through the YSZ electrolyte to the anode. At the anode-electrolyte interface, oxygen ions recombine to produce molecular oxygen. The water-gas shift reaction (WGSR) influences the H_2/CO ratio at higher temperatures. At the high operating temperatures investigated in this study, the water gas shift reaction is assumed to be at thermodynamic equilibrium. Accordingly, WGSR kinetics are not explicitly modeled; instead, equilibrium constraints are applied to determine the cathode gas-phase composition in conjunction with the electrochemical reduction of CO_2 and H_2O [51,67]. This assumption is widely adopted in high-temperature SOEC co-electrolysis modeling, where gas-phase reactions are significantly faster than electrochemical processes. The model integrates experimentally validated degradation mechanisms, including nickel particle coarsening, LSM-YSZ delamination, electrolyte phase transitions, oxide scale growth on interconnects, and the protective effects of LSC coatings to mitigate chromium volatilization and contact resistance. The model considered steady-state, isothermal operation with ideal gas behavior, uniform current density, and uniform reactant distribution at the electrode, while neglecting contact resistance and additional mechanical failures [68,69]. Gas transport was considered through the Stefan-Maxwell equations, and electrochemical kinetics were captured by the Butler-Volmer relation. Degradation was considered as triple phase boundary (TPB) length reduction due to Ni agglomeration, electrolyte phase transitions, delamination, and interconnect oxidation. Consequently, the SOEC operating voltage is defined as the sum of the equilibrium voltage and these overpotentials, as shown in Eq. (1) [12,68].

$$V = Eeq + \eta p\_Vc + \eta_{ohmic,c} + \eta_{ohmic,elect} + \eta p\_Va + \eta_{ohmic,a} \quad (1)$$

Here, V represents the cell voltage, E_{eq} is the equilibrium voltage, ηp_V_c, and ηp_V_a are the polarization overpotentials of the cathode and anode, respectively, $\eta_{ohmic,c}$ and $\eta_{ohmic,a}$ represent the ohmic losses at the cathode and anode, and $\eta_{ohmic,elect}$ denotes the ohmic resistance of the electrolyte.

A schematic of the SOEC configuration, illustrating gas flow, electrochemical reaction sites, oxygen ion transport, and degradation-prone interfaces, is presented in Fig. 1 (b).

This comprehensive model enables realistic prediction of SOEC performance and degradation under co-electrolysis conditions, capturing the interplay of electrochemical performance and multiple degradation pathways over extended operational periods.

The equilibrium or open cell voltage was determined using Eqs. (2) and (3), representing the theoretical minimum electrical potential required to drive the co-electrolysis reactions [10]. This voltage reflects the thermodynamic threshold at which electrochemical splitting of CO_2 and H_2O becomes feasible. Since numerous electrochemical reactions take place at the TPB, the equilibrium voltage is assessed using the mixed theory potential, which is the superposition of potentials arising from the co-electrolysis of CO_2 and H_2O [13,69].

$$E_{H_2} = 1.253 - 0.00024516T + \frac{RT}{2F}\ln\left[\frac{P^I_{H_2}\left(P^I_{O_2}\right)^{0.5}}{P^I_{H_2O}}\right] \quad (2)$$

$$E_{CO} = 1.4671 - 0.0004527T + \frac{RT}{2F}\ln\left[\frac{P^I_{CO}\left(P^I_{O_2}\right)^{0.5}}{P^I_{CO_2}}\right] \quad (3)$$

Here, and E_{CO} are the equilibrium potentials for hydrogen and carbon monoxide electrode reactions, respectively. T is the absolute temperature (K), R is the universal gas constant, and F is the Faraday constant. P^I_{H2}, P^I_{CO}, P^I_{O2}, P^I_{H2O}, and P^I_{CO2} represent the partial pressures of hydrogen, carbon monoxide, oxygen, water vapor, and carbon dioxide, respectively.

Multicomponent gas transport within the porous electrodes is modeled using the Stefan-Maxwell equations under steady-state, isothermal conditions [52,53]. For species in a multicomponent gas mixture, the governing equation is expressed as:

$$\sum_{j\neq i}\frac{xjNi - XiNj}{D_{ij}^{eff}} = \frac{P}{RT}\nabla xi \quad (4)$$

$$D_{ij}^{eff} = \frac{\varepsilon}{\tau}D_{ij} \quad (5)$$

Where xi and xj are the mole fractions of species i and j, Ni is the molar flux of species i, D_{ij}^{eff} is the effective binary diffusion coefficient in the porous electrode, P is the total pressure, R is the universal gas constant, and T is the operating temperature ε is the electrode porosity, τ is the tortuosity factor, and D_{ij} is the bulk binary diffusion coefficient. The boundary conditions are specified as follows: (i) fixed gas compositions and total flow rates at the cathode and anode inlets, (ii) zero diffusive flux at impermeable boundaries such as the electrolyte interface, and (iii) species consumption or generation at the triple-phase boundary determined by local electrochemical reaction rates.

Under CO_2/H_2O co-electrolysis conditions, the equilibrium cell voltage is evaluated using the mixed potential theory [13]. In this framework, the overall equilibrium voltage Eaq is defined as the superposition of the equilibrium potentials associated with the H_2O/H_2 and CO_2/CO redox couples, as expressed in Eqs. (2) and (3), respectively. Thus, the equilibrium voltage used in Eq. (1) is given by Eq. (6):

$$Eeq = E_{H_2} + E_{CO} \quad (6)$$

This formulation assumes that both electrochemical reactions occur simultaneously at the triple-phase boundary under steady-state conditions, and that their contributions to the equilibrium potential are governed by local gas-phase partial pressures. Weighting by partial currents is therefore not required in the present model, consistent with previous high-temperature co-electrolysis studies. The present model focuses on electrochemical performance, mass transport, and time-dependent degradation kinetics under prescribed operating temperatures. Heat conduction and thermo-mechanical stress evolution are not modeled explicitly [54,70]. Thermal effects are incorporated implicitly through temperature-dependent material properties and Arrhenius-type degradation kinetics. The inclusion of fully coupled thermal and mechanical models, which would enable the resolution of local temperature gradients and stress-induced degradation, is beyond the scope of this study and will be addressed in future work.

The present model assumes uniform temperature and stress-free operating conditions and does not explicitly resolve thermal gradients or thermo-mechanical stress evolution. Gas-phase side reactions are treated under equilibrium assumptions, and microstructural evolution within the electrodes is not modeled explicitly. While these assumptions are appropriate for long-term trend analysis, they represent limitations of the current framework. Despite these limitations, the proposed framework provides a physically consistent and computationally efficient tool for assessing long-term degradation behavior in SOEC co-electrolysis systems. The results offer practical insight into the role of interconnect oxidation on voltage degradation and syngas production, which is directly relevant for SOEC stack design, operating strategy optimization, and durability assessment.

2.2. Cathode degradation modelling

A key factor in SOEC longevity is the modeling of material-specific structural changes, which enables the prediction of performance decline over time. This insight allows optimization of operating conditions to reduce degradation and extend cell life. Controlling cathode degradation, primarily caused by Ni sintering and particle growth, is vital for durable and efficient syngas production. Ni agglomeration, driven by the production of Ni_2OH in the rich environment of H_2O, leads to reduced electronic conductivity and decreased TPB length, both of which reduce cell performance [71]. The growth in Ni particle size over time is quantitatively described using Eq. (7), which is used to derive the evolving Ni radius [72,73].

$$rNi = \left| r^7{}_{Ni,0} + C\frac{X_{Ni} \times t}{X_{YSZ} \times A_{YSZ}}\left(\frac{Y_{H_2O}}{Y_{H_2}{}^{0.5}}\right)\exp\left(-\frac{E_{\sin}}{RT}\right)\right|^{1/7} \tag{7}$$

Here, rNi represents the average N_i particle radius after time t, and $rNi_{,0}$ is the initial Ni particle radius. C is an empirical constant, X_{Ni} and X_{YSZ} are the molar fractions of N_i and YSZ in the electrode, and A_{YSZ} is the specific surface area of YSZ. Y_{H2O} and Y_{H2} denote the mole fractions of steam and hydrogen in the gas phase, respectively. E_{sin} is the activation energy for N_i sintering, the other symbols have the same meaning as previously defined.

To further quantify the impact of Ni particle growth on cathode microstructure, Eqs. (8) and (9) have been deployed to describe the evolution of TPB length and Ni particle volume over time, respectively, as the cathode consists of randomly packed spherical particles [71].

$$L_{TPB=}2\pi \times N \times r_{Ni}; L_{TPB,0=}2\pi \times N_0 \times r_{Ni,0} \tag{8}$$

$$V = 4.18 \times Nr^3{}_{Ni}, V_O = 4.18 \times Nr^3{}_{Ni,o} \tag{9}$$

To ensure mass conservation during particle growth, the initial and final Ni particle volumes are equal under constant density conditions. Based on this, Eq. (10) expresses the resulting change in TPB length due to Ni particle growth.

$$\frac{L_{TPB}}{L_{TPB,0}} = \frac{r^2{}_{Ni,0}}{r^2{}_{Ni}} \tag{10}$$

To relate the impact of microstructural degradation to electrochemical performance, the simplified high-field version of the Butler-Volmer equation was employed. Under large overpotential conditions, this approximation simplifies the nonlinear current-voltage relationship into a more tractable exponential form, facilitating analysis of degradation-induced changes in polarization behavior. In this context, the time-dependent behavior of polarization voltage is captured by the following Eq. (16) [71,74]. The electrochemical reaction kinetics at the electrodes are described using the Butler-Volmer formulation. For a generic electrode k ($k = an$ for anode and $k = cat$ for cathode), the local current density is expressed in Eq. (9).

$$j = j_{0,k}\left[\exp\left(\frac{\alpha_{a,k}F\eta_{p,k}}{RT}\right) - \exp\left(\frac{\alpha_{c,k}F\eta_{p,k}}{RT}\right)\right] \tag{11}$$

$$\frac{j}{j_o} = \exp\left(\frac{\alpha.n.F}{RT}\eta_p\right) \tag{12}$$

$$\ln\left(\frac{j}{j_o}\right) = \left(\frac{\alpha.n.F}{RT}\eta_p\right) \tag{13}$$

$$d\ln\left(\frac{j}{j_o}\right) = \left(\frac{\alpha.n.F}{RT}d\eta_p\right) \tag{14}$$

$$d\ln\left(\frac{j}{j_o}\right) = \frac{\alpha.n.F}{RT}\left(\frac{d\eta_p}{dt}\right)dt \tag{15}$$

Where $j_{0,k}$ is the exchange current density, $\alpha_{\alpha,k}$ and $\alpha_{c,k}$ are the anodic and cathodic charge-transfer coefficients, $\eta_{p,k}$ is the polarization overpotential at electrode k, and remaining are the same as mentioned above.

Under typical SOEC operating conditions, the polarization overpotential is sufficiently large such that one exponential term dominates the Butler-Volmer expression. Accordingly, the Butler-Volmer equation can be simplified using the Tafel approximation. For the cathode, where the electrochemical reduction reaction dominates, the second exponential term governs the kinetics, yielding.

$$\ln j - \ln\left(\frac{j_o}{j_{o,0}}\right) = \frac{\alpha.n.F}{RT}\left(\eta_p, i(t) - \eta_p, i(0)\right) \tag{16}$$

where i denote the current density at time t, j is the instantaneous current density, and $j_{0,a}$ denotes the anode exchange current density at the reference state. The term α represents the charge transfer coefficient, n is the number of electrons participating in the electrochemical reaction, and F, R, and T denote the same as described in Eq. (1). $\eta p,_{a(t)}$ and $\eta p,_{a(0)}$ correspond to the anode overpotential at time t and at the initial state, respectively.

Eq. (10) quantifies the rate of change of polarization voltage with respect to time and serves as a key element in modeling how electrochemical performance evolves during prolonged SOEC operation. By linking current density variation to overpotential enables the prediction of degradation effects stemming from microstructural changes such as TPB reduction, active area loss, or interfacial resistance growth.

To establish a direct link between cathode microstructural evolution and electrochemical performance, the polarization voltage is further expressed as a function of TPB length. Eq. (17) describes the polarization voltage as a function of TBP length, taking into account that the exchange current density is directly proportional to its length [71,75] and TPB length change due to Ni particle growth is expressed in Eq. (10).

$$\eta_p, cat(t) = \frac{RT}{\alpha \times n \times F}\ln\left[\ln(j) - \ln\left(\frac{r^2{}_{Ni,0}}{r^2{}_{Ni}}\right)\right] \tag{17}$$

In this equation, $\eta p,cat\ (t)$ represents the cathode overpotential at time t, the other symbols have the same meaning as previously defined.

In modeling the cathode electrical behavior, it is assumed that only the Ni phase undergoes significant structural changes, while YSZ particles remain stable due to their high thermal resistance [71]. The ohmic overpotential on the cathode side at time t, denoted as $U_{s,cat(t)}$, is calculated based on Ohm's law as follows Eq. (18) [76]. Where d_{cat} represents the thickness of the cathode and σ_{cat} represents the conductivity of the cathode.

$$U_{s,cat}(t) = \frac{d_{cat}}{\sigma_{cact}} \times j \tag{18}$$

2.3. Electrolyte degradation modelling

In addition to cathode side effects, degradation also occurs within the electrolyte, impacting its ionic conductivity over time. Electrolyte degradation driven by such material-specific structural transformations plays a significant role in the overall performance decline of SOECs. Accurately modeling these long-term effects is therefore essential for predicting performance losses, optimizing durability, and ensuring stable and efficient syngas production. The reduction in ionic conductivity occurs because YSZ undergoes a phase transition from cubic to tetragonal under high temperatures and reducing conditions, a process driven by cation diffusion [77,78]. This gradual decrease in electrolyte conductivity ($U_{s,El}$) results in an increase in ohmic voltage, as expressed by Ohm's law Eq. (19). The time-dependent ionic conductivity of the electrolyte is accounted for using the established model from [78–80], which is calculated using Eq. (20), where the time constant *(τ),* a function of dopant radius, serves as an indicator of structural stability. In the equation below, *dEl* and *σcat* represent the thickness and conductivity of the electrolyte, respectively. *σEl,0* is the initial ionic conductivity, *σEl,∞* is the stabilized conductivity after long-term aging, and *τ* is the characteristic time constant associated with cation diffusion and phase stabilization in YSZ. The value of depends on the dopant radius and temperature, as reported in [78–80].

$$Us_{,El}(t) = j\frac{d_{El}}{\sigma_{El}(t)} \tag{19}$$

$$\sigma El(t) = \sigma El,\infty + (\sigma El,_0 - \sigma El,\infty)\exp\left(-\frac{t}{\tau}\right) \tag{20}$$

2.4. Anode degradation modelling

Beyond electrolyte degradation, structural instability at the anode contributes significantly to the limited durability of SOECs under high-temperature operation. One major issue is the delamination of LSM-YSZ anodes, primarily caused by three degradation mechanisms: particle coarsening, chromium contamination, and the formation of lanthanum zirconate [69,81]. These mechanisms compromise the electrode-electrolyte interface, necessitating deeper investigation into the microstructural evolution of the anode under co-electrolysis conditions. Modeling these interactions, especially how gas composition influences structural degradation, offers predictive insights for minimizing performance loss and guiding more durable anode designs.

At the anode interconnect interface, chromium within the alloy oxidizes under high-temperature conditions, leading to the formation of a chromium oxide scale (Cr_2O_3), at the anode-interconnect interface as described by Reaction (21) and illustrated in Fig. 2 [60,82,83].

$$2Cr^{\circ} + 1.5\ O_2 \rightarrow Cr_2O_3 \tag{21}$$

This oxide layer, while protective, increases electrical resistance and contributes to additional ohmic overpotentials, ultimately reducing SOECs efficiency. These overpotentials negatively impact overall system efficiency, making interconnect degradation a concern for long-term SOECs performance [68].

To evaluate the long-term impact of this degradation, the growth of the chromium oxide scale (d_{COS}) is modeled based on the diffusion of Cr^{3+} and O^{2-} ions through the scale. The evolution of the oxide layer is described using the Wagner parabolic oxidation kinetics, as reported in Eq. (22), which consists of a weight gain rate (Kg) and an activation energy (E_{cos}) modified by the universal gas constant (R) and absolute temperature (T). This growth is also influenced by the initial size ($Xo_{,COS}$), density (ρcos) of the scale, and growth rate that depends exponentially on temperature via the Arrhenius term exp ($-E_{cos}$/RT) [83,84]. As the oxide layer thickens, it increases interfacial resistance. This effect was quantified through Eq. (24), which links to rising ohmic losses during SOEC operation [85]. The growth of the chromium oxide scale introduces an additional ohmic resistance at the anode interconnect interface. The area-specific resistance of the chromium oxide scale represents this contribution, $R_{COS,}$ which is defined in Eq. (15). Where d_{cos} is the time-dependent oxide scale thickness, and σ_{cos} is the temperature-dependent electrical conductivity of Cr_2O_3, expressed using an Arrhenius relation as reported in [12,60]. The resistance is treated as an area-specific resistance ($\Omega \cdot cm^2$), assuming uniform oxide growth and ideal interfacial contact over the active cell area. The growth of the chromium oxide scale is modeled using Wagner's parabolic oxidation law, which assumes diffusion-controlled growth of a compact and adherent oxide layer under isothermal conditions.

$$d^2{}_{COS(t)} = \frac{K_{g.COS} \times t}{\left(X_{o,COS} \times \rho_{COS}\right)^2}\exp\left(-\frac{Ecos}{RT}\right) \tag{22}$$

$$R_{\cos}(t) = \frac{d_{\cos}(t)}{\sigma_{\cos}(T)} \tag{23}$$

$$Us_{,An(t)} = \mathrm{R_{cos}} \times \mathrm{j} \tag{24}$$

Alongside chromium oxidation, performance decline in SOECs is also driven by microstructural changes in the anode, especially at the critical electrolyte interface region. At high temperatures, the anode microstructure, particularly near the electrolyte/anode interface, tends to be coarser and denser, leading to a decrease in the TPB length on the anode side [62]. The degradation of LSM-YSZ is primarily attributed to the coarsening of the LSM phase, as YSZ coarsening occurs very slowly and is thus considered negligible [86,87]. This LSM coarsening happens due to the diffusion of Mn^{2+} ions along the LSM surface toward the LSM-YSZ interface, where they interact with active TPB sites [62,81]. The movement of these diffusing particles was represented through a

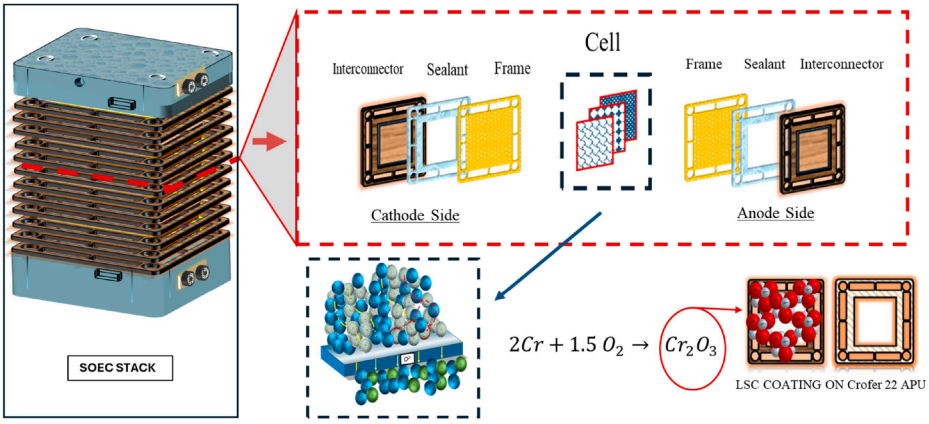

Fig. 2. Summarize the materials and degradation phenomenon in order to facilitate understanding.

one-dimensional mass transport model using Fick's second law, Eq. (25), with the TPB length serving as a measure of the concentration of the diffused species.

$$\frac{\partial}{\partial t}L_{TPB} = D_{LSM}\frac{\partial^2}{\partial x^2}L_{TPB} \tag{25}$$

$$\frac{L_{TPB}}{L_{TPB,0}} = 1 - 2 \times \left(\frac{t \times D_{LSM}}{\pi}\right)^2 \tag{26}$$

To capture the cumulative impact of electrochemical and transport-related degradation, the polarization voltage at the anode was calculated by combining Eqs. (19) and (26) into a single expression, which is represented in Eq. (27). This process involves integrating the relevant electrochemical and transport factors from both Equations to obtain a measure of the voltage required to overcome the polarization effects at the anode. This combined Equation provides a more accurate understanding of the voltage characteristics under different operating conditions. Where D_{An} represents the surface diffusion of the anode, the other symbols have the same meaning as previously described.

$$U_{p,An}(t) = \frac{RT}{\alpha \times n \times F}\left[\ln(j) - \ln 1 - 2 \times \left(\frac{t \times D_{An}}{\pi}\right)^{1/2}\right] \tag{27}$$

2.5. Process efficiences analysis

The degradation rate serves as a critical metric for assessing the performance of the SOEC stack, while syngas production efficiency is a primary measure of the overall system effectiveness. For sustained, high-efficiency operation, it is essential to consider both factors. In this section, the validated model is applied to forecast the SOECs syngas production and electrochemical performance over time. A process efficiency analysis of the intended lifespan for SOEC stacks is carried out after 50,000 h of operations [88].

To quantify these performance metrics, Eq. (28) calculates the average degradation rate of the SOEC over time, in terms of cell voltage variations [89,90] where ΔU is the relative voltage degradation, $U(t_0)$ is the initial voltage at time t_0, and $U(t)$ is the voltage at a later time t. Meanwhile, Eq. (29), derived from the Faraday law, estimates the reactant conversion (RC) fraction, which directly relates to syngas production efficiency [10,91]. Where I is the total current, n is the number of electrons transferred per mole of reactant, F is the Faraday constant, N_{in} is the molar inlet flow rate of the reactant, A_{cell} is the active cell area, N_{cell} is the number of cells, and j is the operating current density.

$$\Delta U = \frac{U(t) - U(t_0)}{U(t_0)} \tag{28}$$

$$RC = \frac{I}{n \times F \times N_{in}} = \frac{A_{cell} \times N_{cell} \times j}{n \times F \times N_{in}} \tag{29}$$

In this study, the electrochemical performance related to syngas formation is quantified using reactant conversion fractions derived from Faraday's law. It is noted that these quantities represent the effectiveness of electrochemical conversion rather than thermodynamic or energy efficiencies. Accordingly, the term "conversion fraction" is used to describe the fraction of supplied reactants converted to H_2 and CO via electrochemical reactions.

For clarity, Table 1 summarizes the oxidation kinetic parameters used in the model for uncoated and LSC-coated ferritic stainless-steel interconnects, together with their literature sources. This comparison highlights the effectiveness of the LSC coating in suppressing chromium oxide scale growth and reducing the associated area-specific resistance.

Fig. 3. illustrates the effect of surface coating on chromium oxide scale growth after long-term oxidation at 1123 K for 1000 h. For the coated interconnect, the coating microstructure remains stable during annealing, while a thin and continuous oxide scale forms at the steel–coating interface, with a thickness of approximately 2–3 μm (Fig. 3(a)).

Table 1
Comparison of oxidation kinetic parameters for uncoated and LSC-coated interconnects.

Parameter	Uncoated (Cn) Interconnector	Coated (Ct) Interconnecttor	Unit	Source
Weight Gain Rate of Growth	2.40 * 10^{-9}	1.15×10^{-10}	$g^2/cm^4.hr$	[82]
Parabolic rate constant	18.9	16.1	10^{14} kp/ $g^2cm^2.s^-$	
K_p (Ct) /K_p(Un)	0.85		-	
Oxide Scale thickness	2–3	10	μm	[92]
Growth Law	Parabolic	Parabolic (Suppressed Rate)	-	

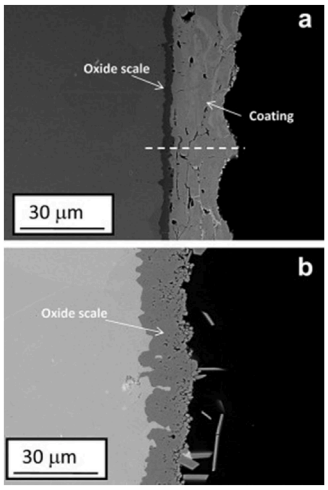

Fig. 3. The microstructure of LSM-coated (a) and uncoated (b) Crofer 22 APU after oxidation at 1123 K for 1000 h in O_2. The location of the EDX linescan is indicated in Fig. 3a by a dashed line. (Reproduced with permission from Ref. [82]. Copyright 2012, Elsevier Ltd).

In contrast, the uncoated steel develops an oxide scale exceeding 10 μm under identical conditions (Fig. 3(b)). This substantial reduction in oxide thickness confirms the protective role of the coating and justifies the use of distinct parabolic oxidation rate constants for coated and uncoated interconnects in the present model [82].

3.0. Results and discussion

3.1. Model validation

The developed SOEC framework was validated against published experimental data sets to assess both performance and degradation predictions. Emphasis was placed on long-term co-electrolysis studies, ensuring that simulated voltage trends, syngas yields, and degradation rates closely aligned with reported experimental results, thereby confirming the model's reliability. After its validated accuracy and robustness makes it a reliable tool for conducting further parametric analyses aimed at improving SOEC performance and degradation over the period. Therefore, the model was used for further sensitivity analysis.

3.1.1. Model validation for SOEC performance analysis

To ensure reliability, the SOEC performance model was validated using experimental data reported by Ciniti et al. [93]. In their study, a stack comprising four planar cells, was operated under CO_2/H_2O co-electrolysis mode. Detailed stack specifications and test parameters applied during validation are listed in Table 2.

Table 2
Performance metrics and laboratory testing parameters [93].

Parameter	UOM	Values
Input gas composition	mol %	H_2O:70, CO_2:20, H_2:10
Cathode inlet flow rate	mol/hr	8.50
Thickness of porous cathode	mm	0.008
Anode inlet flow rate	mol/h	8.95
Thickness of porous anode	mm	0.012
Thickness of dense electrolyte	mm	0.008
Stack operating temperature	K	1023
Operating pressure	kPa	100
Cell geometric surface area of a single cell	cm^2	100 (10 * 10)
Effective electrode surface area per cell	cm^2	80
Total number of cells in the stack	-	4 × 1

The validation results, presented in Fig. 4, Compare the simulated outlet mole fractions of CO_2, H_2, and CO with experimental data under varying current densities. These comparisons were made based on the conditions specified in Table 2, allowing for an assessment of the model accuracy in predicting the gas composition at different operating points.

The quantitative validation based on percentage deviation further supports the predictive capability of the model. Over the evaluated operating points, deviations remain within 6.0–12.5 % for CO, 3.33–7.41 % for H_2, and 3.33–9.09 % for CO_2. The tight deviation band for H_2 demonstrates that the model accurately describes steam electrolysis contributions and the resulting hydrogen enrichment of the outlet stream under increasing current density. Similarly, the deviation range for CO_2 confirms that the model captures the progressive depletion of CO_2 associated with enhanced electrochemical reduction, with a tendency toward underprediction at higher current density reflected by negative deviations. This behavior is consistent with operating regimes where transport and polarization effects become more influential, leading to local departures from ideal mixing or equilibrium assumptions. CO exhibits the widest deviation range, which is expected because CO is a minor component throughout the operating window and therefore more sensitive to small absolute differences in conversion, local equilibrium, and measurement uncertainty. In co-electrolysis, CO can originate from both direct electrochemical CO_2 reduction and the reverse water-gas shift pathway, so even modest mismatches in the local H_2O/H_2 balance, residence time, or temperature distribution can translate into larger relative deviations in CO fraction compared with the major components.

Despite minor discrepancies as shown in Table 3 the SOEC model demonstrates strong predictive capability for syngas composition profiles. The simulated H_2 and CO concentrations closely follow experimental trends, indicating that the electrochemical degradation framework effectively captures the key reaction and transport phenomena under co-electrolysis conditions.

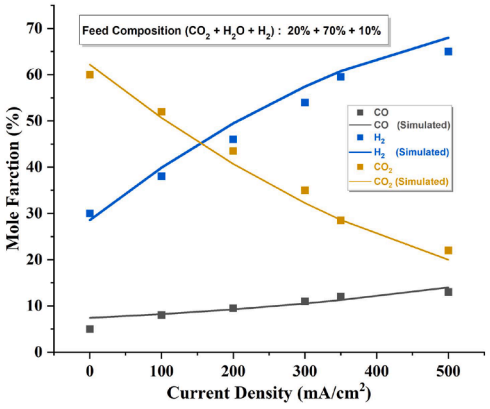

Fig. 4. Model predictions for input feed compositions vs experimental values of output syngas composition.

Table 3
Observation of relative errors.

Current Density (mA/cm^2)	Relative Error (%)		
	H_2	CO	CO_2
0	3.3	14	10.1
100	8.1	12.5	1.9
200	10.1	7.2	5.7
300	14.6	7.6	8.1
400	11.4	5.2	4.1
500	10.2	4.2	3.57

3.1.2. *Model validation for SOEC degradation analysis*

Experimental data reported by Ebbsesn et al. and Sun et al. were used to validate the integrated model for SOEC structural degradation, respectively [21,61]. All operating parameters from these experiments, including cell geometry, gas compositions, flow rates, temperatures, and current densities, were directly applied in the simulations. These, along with the corresponding experimental conditions, are summarized in Table 4. The durability of SOECs during co-electrolysis at both low and high current densities was assessed in a single experiment, with comprehensive specifications provided for model validation.

The model was simulated under the operating conditions specified in Table 4 to generate the results presented in this section. Due to the unavailability of certain input data, values were estimated within reasonable limits, drawing on existing data from the current body of

Table 4
DTU energy conversion SOEC properties and test parameters [21,61] and reference properties for validating SOEC simulations.

Parameter	UOM	Values	Parameter	UOM	Values
Cathode inlet gas ratio ($H_2O/CO_2/H_2$)	mol %	45: 45: 10	System pressure	bar	1.0
Cathode gas flow rate	m^3/h	0.25	Single cell geometric area	cm^2	5 × 5
Cathode layer thickness	μm	10	Effective electrode area	cm^2	16
Cathode porosity	%	40	Number of cells in stack	—	2
Ni volume ratio	—	40	YSZ volume ratio	—	60
Nickel particle radius	μm	4.5	Activation energy for Ni sintering [94]	J/mol	332,000
Initial YSZ particle radius	μm	4	YSZ ionic conductivity activation energy [78,95]	J/mol	80,000
YSZ surface area	m^2/g	0.41	Pre-exponential constant for YSZ [78,95]	S/cm	360,000
Anode inlet gas composition (O_2)	mol %	100	Ionic radius of the YSZ cation [78]	Å	1.01
Anode gas flow rate	L/h	50	Surface diffusivity of LSM [81]	cm2 /hr	1.12×10^{-5}
Anode layer thickness	μm	20	Density of chromium oxide scale (Cr_2O_3) [82,83]	g/cm3	5.255
Anode porosity	%	35	Mass gain rate during Cr_2O_3 scale formation [21,61]	g2 /cm4 . hr	6.84×10^{-10}
LSM to YSZ volume ratio	—	50: 50	Activation energy for Cr_2O_3 scale growth [21,61]	J/mol	220,000
Electrolyte layer thickness	μm	12	Conductivity activation energy for Cr_2O_3 [21,61]	J/mol	86,200
Operating temperature	°C	850	Pre-exponential constant for Cr_2O_3 conductivity [21,61]	S/cm	320,000

literature. These approximations were necessary to complete the model inputs and ensure its applicability under the given operational parameters, which provide the calculated values based on these reasonable assumptions. The agreement between experiment and simulation is supported by the percentage-deviation analysis. At 500 mA cm^{-2}, the deviation lies within 0.90 % to 1.31 %, and at 1000 mA cm-2 it lies within 0.81 % to 1.12 %. These narrow bounds indicate that the model captures both the magnitude of the voltage rise and the rate of degradation over time, without systematic drift relative to the measurements. Minor point-to-point differences are expected in long-duration SOEC testing due to operational variability and transient effects (temperature fluctuations, gas-composition variations, and contact resistance changes), yet the deviations remain close to unity across the full duration. Fig. 5 and Table 5, shows a strong agreement between the model predictions and experimental observations, with the discrepancies consistently remaining below 2.0 %. This indicates that the model accurately replicates the experimental results, with minimal error.

The results presented in this section were obtained by simulating and developing a model using the ACM. This model effectively captures the structural degradation behavior of the SOEC stack across a range of input conditions.

3.2. Sensitivity analysis

After the model validated accuracy, a sensitivity analysis was conducted to investigate how key operating parameters influence both syngas production efficiency and the degradation rate of the SOEC stack. Specifically, the study examined the effects of varying intake temperatures, current densities, and feed ratios. These parameters were selected due to their significant influence on electrochemical reactions, heat distribution, and gas-phase transport within the system. By systematically altering these inputs, the analysis aimed to gain a deeper understanding how the designed SOEC system behaves under realistic operating conditions. The following discussion provides detailed insights into how each of these operating variables impacts the degradation trend, stack voltage, and overall syngas production efficiency over time.

3.2.1. Impact of current density on degradation and syngas efficiency

Current density was selected as a primary sensitivity parameter because it directly influences reactant conversion rates, syngas yield, and degradation progression in SOECs. For this analysis, all other operating conditions were fixed to isolate the impact of current density, cathode flow rate of 0.36 m^3/h, feed composition of 45 % CO_2, 45 % H_2O, and 10 % H_2, operating temperature of 800 °C, and cell properties listed in Table 4. A range of 500–1000 mA/cm^2 was investigated to represent typical industrial and high-load operating regimes [96]. Fig. 6

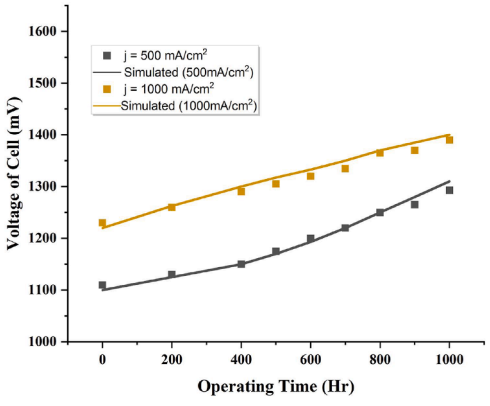

Fig. 5. Comparison of model predictions with experimental measurements of SOEC degradation.

Table 5
Observation of relative errors.

Operating Time (Hrs)	Relative Error (%)
0	0.85
200	0.80
400	0.41
600	0.78
800	1.14
1000	0.52

illustrates that after 50,000 h of operation, efficiency declined from 55.4 % to 36.8 % at 500 mA/cm^2 and from 53.5 % to 23.0 % at 1000 mA/cm^2, corresponding to efficiency loss rates of 0.39 %/1000 h and 0.61 %/1000 h, respectively. Voltage degradation followed the same trend, with average increases of 2.42 % and 5.57 % per 1000 h at the lower and higher current densities. Elevated current densities accelerated ohmic and polarization losses, consistent with prior experimental findings by Graves et al. [14] and Sun, et al. [61], where high current operation intensified Ni coarsening, TPB loss, and interconnect oxidation. This trade-off between high initial output and long-term stability underscores the need for optimized current density selection and material/coating strategies to maintain durability under industrial-scale loads.

3.2.2. Impact of temperature on syngas efficiency and degradation

Temperature was selected for sensitivity analysis due to its strong influence on adsorption, mass transfer, and electrochemical kinetics in SOECs [5]. Simulations were run from 750–850 °C at 1000 and 1500 mA/cm^2 fixed gas composition and flow, Table 3, to assess trade-offs between conversion efficiency and durability. Higher temperatures reduced equilibrium voltage and increased initial syngas efficiency Fig. 7(a) and (b) due to faster electrochemical reaction rates, consistent with Menon et al. [95]. However, long-term performance declined faster at elevated temperatures: at 1000 mA/cm^2, efficiency dropped from 54.0 % to 37.4 % at 850 °C (5.86 %/1000 h), from 53.0 % to 41.1 % at 750 °C (4.06 %/1000 h). This accelerated degradation is linked to the temperature-driven Ni agglomeration (described by Equation (04), which models the coarsening rate of Ni particles) and Cr_2O_3 scale growth Eq. (12), which intensifies with heat and reduces effective TPB length. Results confirm that while higher temperatures improve short-term efficiency, lower-temperature operation better supports long-term SOEC durability.

3.3.3. Impact of feed gas composition and flow rate on degradation and syngas efficiency

Feed gas composition and cathode flow rate are critical parameters influencing both syngas quality (H_2/CO ratio) and SOEC long-term performance. For Fischer-Tropsch synthesis (FTS), the optimal H_2/CO ratio is 1.7–2.1 [97], making it essential to evaluate how inlet gas composition and flow rate affect performance and durability. In this case study, the SOEC was operated at 750 °C and 1000 mA/cm^2, with two cathode feed compositions: Feed 1 (F1: 30 % CO_2, 60 % H_2O, 10 % H_2) and Feed 2 (F2: 60 % CO_2, 30 % H_2O, 10 % H_2), both at a flow rate of 0.36 m^3/h.

Over 50,000 h of operation, H_2/CO production efficiency for F1 decreased from 53.0 % to 41.9 % (average degradation rate 4.21 %/1000 h), while for F2 it dropped between 50.8 % to 39.65 % (3.08 %/1000 h). As shown in Fig. 8, Higher H_2O fractions reduced the operating voltage and increased the H_2/CO ratio, enhancing efficiency. Conversely, higher CO_2 fractions increased operating voltage due to greater concentration overpotentials from slower CO_2 diffusion compared to H_2O [14]. Flow rate variation revealed that increasing feed velocity improved efficiency by increasing reactant supply to the TPB, consistent with Menon et al. [95]. However, excessively high flow rates provided no additional benefit due to current density-limited conversion, potentially wasting feedstock and increasing raw material costs.

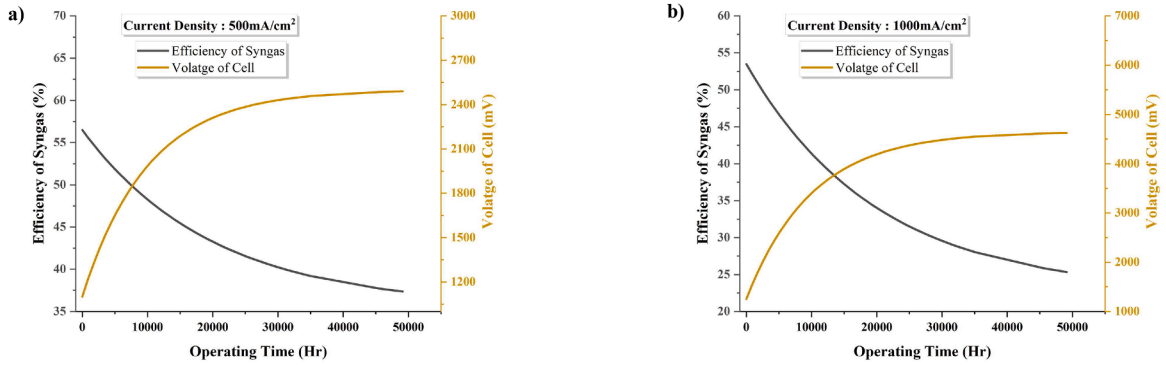

Fig. 6. Efficiency of syngas and Stack cell voltage as a function of operating time (a) At 500mA/cm^2 and (b) At 1000mA/cm^2.

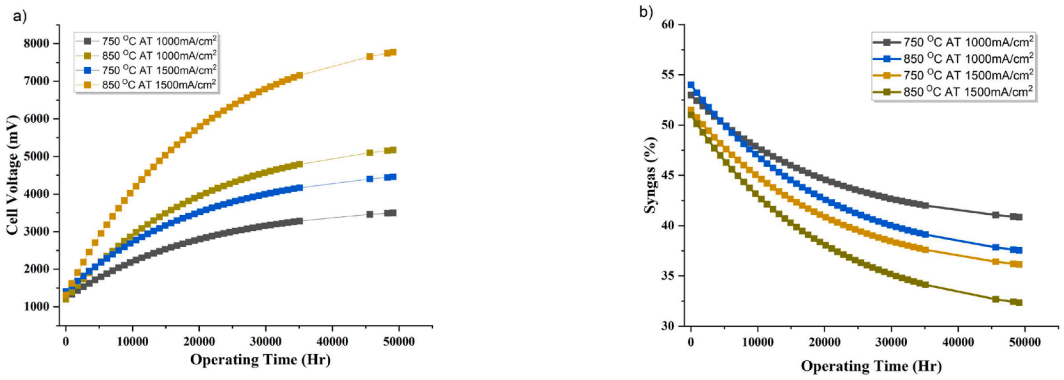

Fig. 7. Effect of temperature (a) SOEC stack voltage and (b) syngas efficiency.

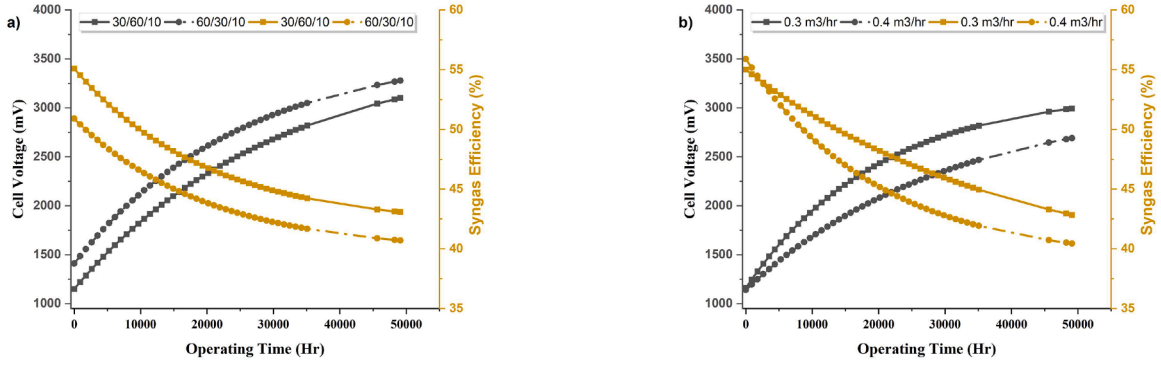

Fig. 8. (a) Effects of feed gas composition on stack voltage and (b) Effects of feed Flow rate on stack voltage.

The long-term trends suggest that high H_2O concentrations, while initially improving efficiency, may accelerate degradation via Ni re-oxidation or enhanced Ni sintering at the cathode [94]. These results highlight the trade-off between short-term efficiency gains and long-term stability.

3.3. Impact of structural degradation on SOEC long-term operation

This section was included in this study to investigate the causes of structural damage in SOEC materials. Based on the findings, a strategic approach was developed to improve the durability and syngas efficiency of SOECs under given conditions.

3.3.1. Structural degradation of cathode

In this study, all material components were considered stable, with only the component under investigation subjected to variation. The operating conditions were set at 750 °C, 1000 mA/cm^2, with a gas mixture consisting of 30 % CO_2, 60 % H_2O, and 10 % H_2, along with a cathode flow rate of 0.36 m^3/hr. The properties of the materials used in the base scenario are detailed in Table 2 and Table 4. Fig. 9 shows the influence of Ni particle growth on cathode behavior. As particles coarsen, the TPB length decreases, reducing electronic conductivity. This degradation results in higher overpotential and reduced SOEC performance. The results show that Ni radius increases from 4.50 to 5.18 μm after 50,000 h, lowering the TPB length ratio (L_{TPB}/L_{TPB_o}) from 1.00 to 0.747 and the electronic conductivity from 1292 to 1029 S/cm. The cathodic overpotential increases from 17.8 to 30.65 mV due to this Ni agglomeration, which interprets to an average rate of cell degradation of 0.026 % per 1000 h.

3.3.2. Structural degradation of electrolyte

The phase change of the electrolyte from cubic to tetragonal lattice

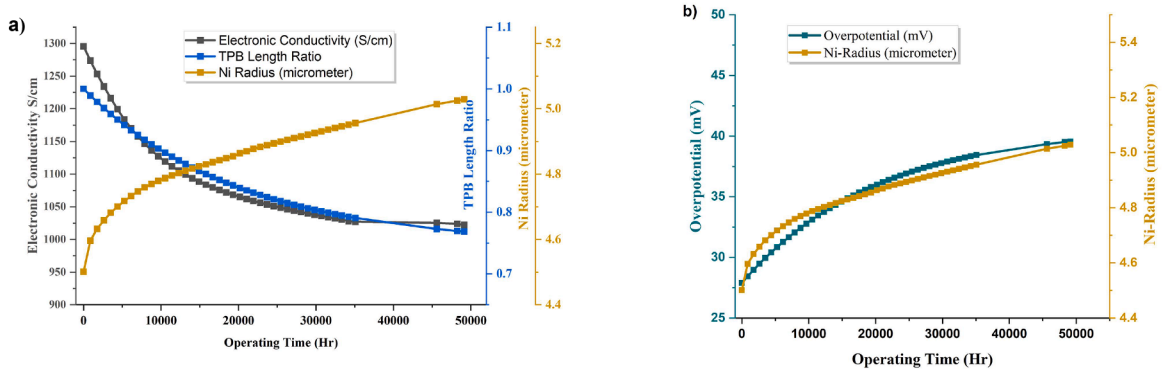

Fig. 9. (a) Evolution of TPB length and conductivity and (b) Variation in cathodic overpotential.

and its influence on the electrolyte overpotential and ionic conductivity are shown in Fig. 10. During the first one thousand hours of operation, the ionic conductivity drops quickly from 0.0371 to 0.0292 S/cm and then remains constant at 0.0288 S/cm. This is consistent with YSZ ionic conductivity data obtained with varying Y_2O_3 mol % [83]. After 50,000 h of operation, the corresponding overpotential exhibits a minor alteration in pattern, ranging from 48.8 to 63.93 mV, having a degradation rate of 0.07 %/1000 h. The short-range order-disorder change occurring in the crystal lattice is the cause of the drop in YSZ conductivity during the first one thousand hours. These structural rearrangements disrupt the regular pathways for oxygen ion migration, thereby hindering ionic transport and leading to a measurable decrease in conductivity. Once equilibrium is achieved, YSZ conductivity stays constant with oxygen ions still flowing easily after the phase transformation [98].

3.3.3. *Structural degradation of anode*

Over time, both ohmic and polarization voltages increase, as shown in Fig. 11. primarily due to two degradation mechanisms: the thickening of the chromium oxide scale (COS) and the coarsening of the LSM-YSZ phase. The COS layer, growing between 0 and 5.7 $\times$ 10^{-3} cm over 50,000 h, causes the ohmic voltage to rise between 0 and 2290 mV due to increased internal resistance. Simultaneously, the TPB length decreases over the range of 1.0 to 0.129, while the polarization voltage increases from 18 to 333.6 mV. The TPB degrades at a rate of 1.76 % per 1000 h, identifying LSM-YSZ anode delamination as the dominant long-term degradation factor in SOECs.

To mitigate this, the rate of COS growth can be effectively slowed by applying an antioxidant coating to the anode side connection surface. Applying a $La_{0.8}Sr_{0.2}CoO_3$ coating on a Crofer 22 APU interconnect, for instance, significantly reduces the COS growth rate ($Kg_{,COS}$) from 2.42 $\times$ 10^{-9} to 1.10 $\times$ 10^{-10} ($g^2.cm^{-4}.hr^{-1}$) [82]. This slower development rate causes the COS thickness to drop considerably after 50,000 h of operation, to just 1.2 $\times$ 10^{-4} cm as seen in Fig. 10 (a). As a result, the increased ohmic and polarization voltages caused by the LSM-YSZ material were significantly reduced, with TPB degradation improving by 40.34 %, and the ohmic and polarization voltages decreasing by 57.6 % and 60.4 %, respectively, as shown in Fig. 10 (b).

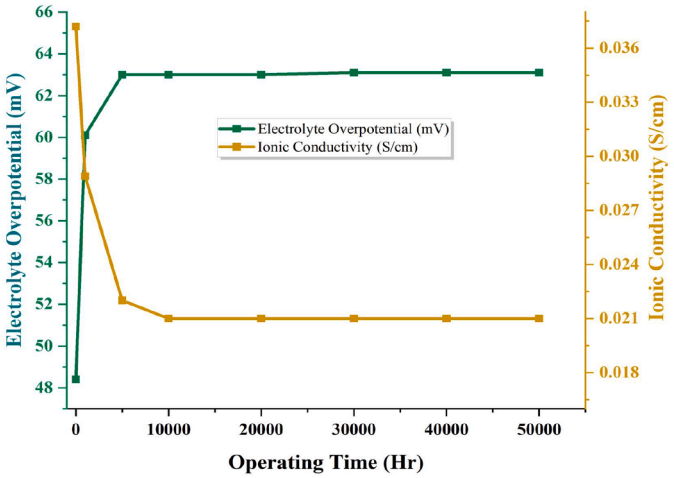

Fig. 10. YSZ electrolyte phase transition and its effect on cell performance.

3.4. *Overall performance and durability of SOEC*

The impact of structural changes in the Ni-YSZ/YSZ/LSM-YSZ material system on syngas production efficiency and SOEC performance degradation is shown in Fig. 12. For the baseline SOEC operating at 1000 mA/cm^2, syngas generation performance drops from 51.2 % down to 22.2 % over 50,000 h. This decline is associated with various degradation mechanisms, including a 0.55 %/1000 hrs reduction in TPB length due to Ni agglomeration, negligible degradation from the YSZ electrolyte phase transition, and a dominant 1.76 %/1000 hrs degradation rate attributed to anode delamination. These factors collectively contribute to the observed performance decline over time.

Following optimization of operating conditions and material enhancements, the total degradation rate is substantially reduced to 0.70 %/1000 hrs., with syngas production efficiency maintained between 53.1 % and 45.5 % after 50,000 h. These results underscore the critical importance of operating SOECs within optimal temperature ranges and tailored cathode feed compositions to minimize degradation and maximize syngas quality and yield. Furthermore, selecting appropriate compositions for the cathode and anode, coupled with antioxidant coatings on interconnects, is vital to reaching low degradation rates. This demonstrates that SOECs employing conventional, cost-effective materials can achieve sufficient long-term stability for large-scale applications. Despite the fact that the measured rate of degradation of 0.70 %/1000 hrs. meets commercial viability thresholds (targeting <1.0 %/1000 hrs), further investigations are required to address other degradation mechanisms, including mechanical failures and component-level issues such as sealing integrity.

4.0. Conclusion

An integrated planar SOEC model was developed in ACM to simulate the electrochemical performance and long-term degradation during high-temperature CO_2/H_2O co-electrolysis. Model validation against experimental measurements demonstrates reliable predictive performance for both composition and durability. For syngas composition, the model reproduces the current-density-dependent trends of CO, H_2, and CO_2, with percentage deviations confined to 6.0–12.5 % (CO), 3.33–7.41 % (H_2), and 3.33–9.09 % (CO_2) across the tested operating points. For degradation, the model accurately captures the progressive

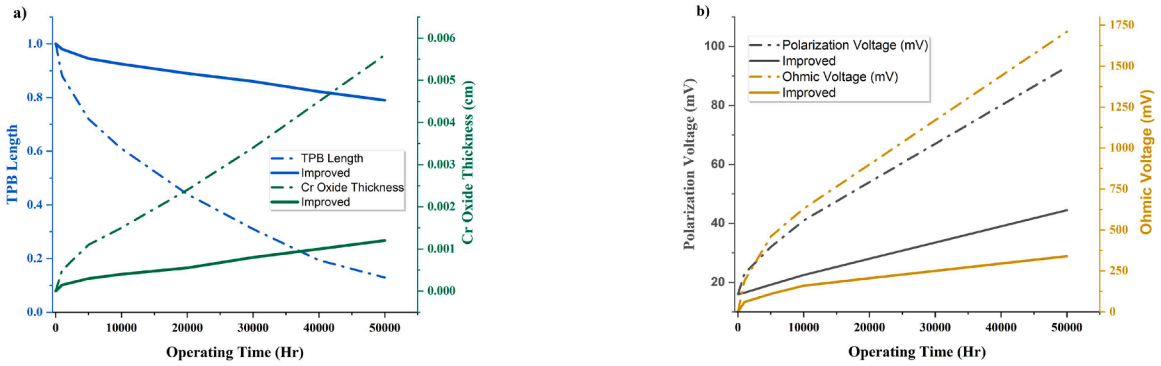

Fig. 11. Impact of Degradation on (a) Ohmic and polarization voltages, (b) Cr oxide growth and TPB interface length.

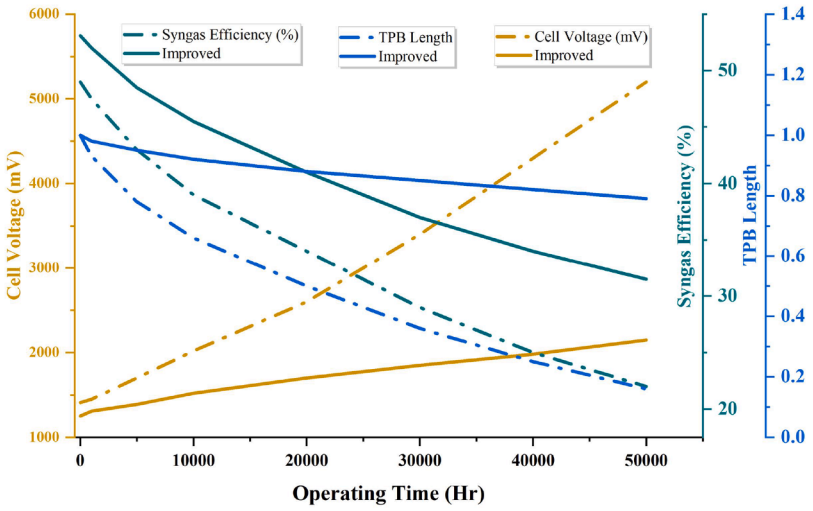

Fig. 12. Comparison of syngas generation efficiency, SOEC degradation, and TPB length degradation rate for the original and upgraded parameter sets.

increase in cell voltage with operating time at 500 and 1000 mA cm^{-2}, with deviations restricted to 0.90–1.31 % and 0.81–1.12 %, respectively. These results confirm that the proposed framework predicts both instantaneous syngas quality and long-term performance decay within a single unified platform. Validated against experimental polarization data across current densities from 100 to 1000 mA/cm^2, the model quantifies the effects of operating conditions and material degradation on both syngas production efficiency and cell durability. Simulation results highlight that while higher current densities and temperatures boost initial performance, they also accelerate voltage increases and efficiency losses due to intensified degradation mechanisms, most notably interconnect oxidation and LSM-YSZ anode delamination. Over 50,000 h of operational period at 750 °C and 1A/cm^2, the TPB length degrades at a rate of 1.76 % per 1000 h. To address this, the implementation of a single-layer LSC coating was applied to Crofer 22 APU interconnects, serving as an effective oxygen transport barrier. This modification reduced anode corrosion and decreased the TPB length degradation rate by 40.34 %, thereby significantly improving SOEC stability. These findings demonstrate a synergistic approach that combines predictive modeling with advanced material engineering to optimize SOEC durability and performance, paving the way for their practical deployment in sustainable industrial syngas production. Future work will extend the present model to include coupled thermal and mechanical effects, non-equilibrium reaction kinetics, and spatially resolved stack-level simulations, enabling a more comprehensive assessment of degradation mechanisms under realistic operating conditions.

CRediT authorship contribution statement

Abrar Ahmad: Writing – original draft, Visualization, Validation, Methodology, Investigation, Formal analysis, Data curation, Conceptualization. **Serene Sow Mun Lock:** Supervision, Project administration, Investigation, Funding acquisition, Conceptualization. **Lam Ghai Lim:** Validation, Data curation, Writing – review & editing. **Irene Sow Mei Lock:** Visualization, Validation. **Grazia Leonzio:** Writing – review & editing. **Chung Loong Yiin:** Writing – review & editing. **Chrisminder Dain:** Conceptualization, Funding acquisition.

Declaration of competing interest

The authors declare that they have no known competing financial interests or personal relationships that could have appeared to influence the work reported in this paper.

Acknowledgements

We want to acknowledge the financial support provided by Yayasan Universiti Teknologi PETRONAS (YUTP) Fundamental Research Grant (Cost Centre: 015LC0-498 and 015LC0-618).

Data availability

Data will be made available on request.

References

[1] P.D. Patil, et al., Bioconversion of lignocellulosic residues into hydrogen, Sustain. Bioconversion Waste Value Added Prod. (2021) 59–80.
[2] I.-I.E. Agency, CO2 emissions – global energy review 2025 – analysis [cited 2025; Available from: https://www.iea.org/reports/global-energy-review-2025/co2, 2025.
[3] M.N. Dods, et al., Deep CCS: moving beyond 90% carbon dioxide capture, Environ. Sci. Technol. 55 (13) (2021) 8524–8534.
[4] S.S.M. Lock, et al., Modeling, simulation and economic analysis of CO2 capture from natural gas using cocurrent, countercurrent and radial crossflow hollow fiber membrane, Int. J. Greenh. Gas Control 36 (2015) 114–134.
[5] M. Filonchyk, et al., Greenhouse gases emissions and global climate change: examining the influence of CO2, CH4, and N2O, Sci. Total Environ. (2024) 173359.
[6] C. Bu, et al., Oxy-fuel combustion of a single fuel particle in a fluidized bed: char combustion characteristics, an experimental study, Chem. Eng. J. 287 (2016) 649–656.
[7] M.M. Gui, et al., Photo-driven reduction of carbon dioxide: a sustainable approach towards achieving carbon neutrality goal, Front. Chem. Eng. 3 (2021) 744911.
[8] A.D.N. Kamkeng, et al., Transformation technologies for CO2 utilisation: current status, challenges and future prospects, Chem. Eng. J. (2021) 409.
[9] A. Al Harthi, et al., Criteria and cutting-edge catalysts for CO_2 electrochemical reduction at the industrial scale, J. CO2 Util. 83 (2024) 102819.
[10] X. Hou, et al., Syngas production from CO2 and H2O via solid-oxide electrolyzer cells: fundamentals, materials, degradation, operating conditions, and applications, Chem. Rev. 124 (8) (2024) 5119–5166.
[11] S.-B. Yu, et al., Syngas production in high performing tubular solid oxide cells by using high-temperature H2O/CO2 co-electrolysis, Chem. Eng. J. 335 (2018) 41–51.
[12] Y. Zheng, et al., A review of high temperature co-electrolysis of H 2 O and CO 2 to produce sustainable fuels using solid oxide electrolysis cells (SOECs): advanced materials and technology, Chem. Soc. Rev. 46 (5) (2017) 1427–1463.
[13] J.P. Stempien, et al., Physical principles for the calculation of equilibrium potential for co-electrolysis of steam and carbon dioxide in a solid oxide electrolyzer cell (SOEC), Electrochim. Acta 147 (2014) 490–497.
[14] C. Graves, S.D. Ebbesen, M. Mogensen, Co-electrolysis of CO2 and H2O in solid oxide cells: performance and durability, Solid State Ion. 192 (1) (2011) 398–403.
[15] Y. Xu, et al., Optimal design and performance enhancement based on field synergy theory in a solid oxide electrolysis cell with blockage flow channel, Electrochim. Acta 479 (2024) 143842.
[16] M.B. Mogensen, et al., Ni migration in solid oxide cell electrodes: review and revised hypothesis, Fuel Cells 21 (5) (2021) 415–429.
[17] T. Liu, et al., Degradation mechanisms and protective coatings for ferritic stainless-steel interconnects of solid oxide fuel cells: a review, Mater. Today Commun. 41 (2024) 110802.
[18] A.V. Virkar, Mechanism of oxygen electrode delamination in solid oxide electrolyzer cells, Int. J. Hydrog. Energy 35 (18) (2010) 9527–9543.
[19] W. Gu, et al., High temperature phase transitions in solid state electrolytes, Curr. Opin. Electrochem. 46 (2024) 101537.
[20] X. Shao, et al., Review of factors affecting the performance degradation of Ni-YSZ fuel electrodes in solid oxide electrolyzer cells, J. Power Sources 609 (2024) 234651.
[21] S.D. Ebbesen, et al., Durable SOC stacks for production of hydrogen and synthesis gas by high temperature electrolysis, Int. J. Hydrog. Energy 36 (13) (2011) 7363–7373.
[22] J.W. Fergus, Metallic interconnects for solid oxide fuel cells, Mater. Sci. Eng.: A 397 (1–2) (2005) 271–283.
[23] T.-L. Wen, et al., Material research for planar SOFC stack, Solid State Ion. 148 (3–4) (2002) 513–519.
[24] M. Bianco, et al., Chapter 7 - lifetime issues for solid oxide fuel cell interconnects, in: N.P. Brandon, E. Ruiz-Trejo, P. Boldrin (Eds.), Solid Oxide Fuel Cell Lifetime and Reliability, Academic Press, 2017, pp. 121–144.
[25] J. Mao, et al., Progress in metal corrosion mechanism and protective coating technology for interconnect and metal support of solid oxide cells, Renew. Sustain. Energy Rev. 185 (2023) 113597.
[26] W.Z. Zhu, S. Deevi, Development of interconnect materials for solid oxide fuel cells, Mater. Sci. Eng.: A 348 (1–2) (2003) 227–243.
[27] K. Hilpert, W.J. Quadakkers, L. Singheiser, Interconnects. Handb. Fuel Cells (2010).
[28] Y. Pan, et al., Effect of pre-oxidation on surface scale microstructure and electrical property of Cu-Fe coated steel interconnect, Corros. Sci. 170 (2020) 108680.
[29] K.H. Jo, et al., Development of a new cost effective Fe–Cr ferritic stainless steel for SOFC interconnect, Int. J. Hydrog. Energy 40 (30) (2015) 9523–9529.
[30] T. Thublaor, S. Chandra-ambhorn, High temperature oxidation and chromium volatilisation of AISI 430 stainless steel coated by Mn-Co and Mn-Co-Cu oxides for SOFC interconnect application, Corros. Sci. 174 (2020) 108802.
[31] B. Timurkutluk, S. Celik, E. Ucar, Effects of solid loading on joining and thermal cycling performance of glass-ceramic sealing pastes for solid oxide fuel cells, Ceram Int. 45 (10) (2019) 12845–12850.
[32] T. Altan, S. Celik, Effect of surface roughness of the metallic interconnects on the bonding strength in solid oxide fuel cells, Int. J. Hydrog. Energy 45 (60) (2020) 35118–35129.
[33] B. Talic, et al., Comparison of MnCo2O4 coated crofer 22 H, 441, 430 as interconnects for intermediate-temperature solid oxide fuel cell stacks, J. Alloys Compd. 821 (2020) 153229.
[34] X. Li, J.-W. Lee, B.N. Popov, Performance studies of solid oxide fuel cell cathodes in the presence of bare and cobalt coated E-brite alloy interconnects, J. Power Sources 187 (2) (2009) 356–362.
[35] X. Wang, et al., Influence of grain orientation on the incipient oxidation behavior of Haynes 230 at 900°C, Mater. Charact. 107 (2015) 33–42.
[36] B. Timurkutluk, et al., Determination of formability characteristics of Crofer 22 APU sheets as interconnector for solid oxide fuel cells, Int. J. Hydrog. Energy 43 (31) (2018) 14638–14647.
[37] Y. Li, et al., Oxidation behavior of metallic interconnects for SOFC in coal syngas, Int. J. Hydrog. Energy 34 (3) (2009) 1489–1496.
[38] P. Huczkowski, et al., Growth mechanisms and electrical conductivity of oxide scales on ferritic steels proposed as interconnect materials for SOFC's, Fuel Cells 6 (2) (2006) 93–99.
[39] Ł. Mazur, T. Brylewski, Electrophoretic deposition and physicochemical properties of Ni- and Fe-doped Cu–Mn spinel coatings enhanced with Ce0.9Y0.1O2 nanoparticles on Fe16Cr ferritic Stainless steel interconnects for SOEC applications, Metall. Mater. Trans. A 55 (12) (2024) 5100–5113.
[40] Z. Zhu, et al., Comparison of Cu–Mn and Mn–Co spinel coatings for solid oxide fuel cell interconnects, Int. J. Hydrog. Energy 47 (87) (2022) 36953–36963.
[41] J. Beyrami, et al., Degradation modeling in solid oxide electrolysis systems: a comparative analysis of operation modes, Energy Convers. Manag.: X 23 (2024) 100653.
[42] N. Shaigan, et al., A review of recent progress in coatings, surface modifications and alloy developments for solid oxide fuel cell ferritic stainless steel interconnects, J. Power Sources 195 (6) (2010) 1529–1542.
[43] K. Wang, et al., Rational design of perovskite anode materials in solid oxide electrolysis cells: machine learning-assisted prediction of thermal expansion coefficients, Ind. Eng. Chem. Res. 64 (21) (2025) 10508–10521.
[44] L.M. Acuña, F.F. Muñoz, R.O. Fuentes, Correlation between structural, chemical, and electrochemical properties of La0.6Sr0.4CoO3–d nanopowders for application in intermediate temperature solid oxide fuel cells, J. Phys. Chem. C 120 (36) (2016) 20387–20399.
[45] Y.-S. Chou, et al., Thermal, mechanical, and electrical properties of LSCo/mullite composite contact materials for solid oxide fuel cells, Int. J. Appl. Ceram. Technol. 17 (5) (2020) 2051–2061.
[46] A.D.N. Kamkeng, M. Wang, Long-term performance prediction of solid oxide electrolysis cell (SOEC) for CO2/H2O co-electrolysis considering structural degradation through modelling and simulation, Chem. Eng. J. (2022) 429.
[47] M. Naeini, J.S. Cotton, T.A. Adams, Data-driven modeling of long-term performance degradation in solid oxide electrolyzer cell system, in: Y. Yamashita, M. Kano (Eds.), Computer Aided Chemical Engineering, Elsevier, 2022, pp. 847–852.
[48] F. Shen, S.A. Ibanez, M.C. Tucker, Dynamic oxidation of (Mn, Co) 3O4-coated interconnects for solid oxide electrolysis cells, Int. J. Hydrog. Energy 48 (86) (2023) 33434–33441.
[49] M. Rao, X. Sun, A. Hagen, Durability of solid oxide electrolysis stack under dynamic load cycling for syngas production, J. Power Sources 451 (2020) 227781.
[50] C. Chatzichristodoulou, et al., Understanding degradation of solid oxide electrolysis cells through modeling of electrochemical potential profiles, Electrochim. Acta 189 (2016) 265–282.
[51] W.-H. Chen, C.-Y. Chen, Water gas shift reaction for hydrogen production and carbon dioxide capture: a review, Appl. Energy (2020) 258.
[52] A. Jungel, I.V. Stelzer, Existence analysis of Maxwell–Stefan systems for multicomponent mixtures, SIAM J. Math. Anal. 45 (4) (2013) 2421–2440.
[53] R. Taylor, R. Krishna, Multicomponent Mass Transfer, John Wiley & Sons, 1993.
[54] E. Lay-Grindler, et al., Degradation study by 3D reconstruction of a nickel–yttria stabilized zirconia cathode after high temperature steam electrolysis operation, J. Power Sources 269 (2014) 927–936.
[55] A.D.N. Kamkeng, M. Wang, Long-term performance prediction of solid oxide electrolysis cell (SOEC) for CO2/H2O co-electrolysis considering structural degradation through modelling and simulation, Chem. Eng. J. 429 (2022) 132158.
[56] Z. Xia, et al., Control-oriented performance prediction of solid oxide electrolysis cell and durability improvement through retard oxygen electrode delamination with reverse operation, Energy Convers. Manag. 277 (2023) 116596.
[57] Reddy, M.J., *Metallic materials for solid oxide fuel cells and electrolysers.* 2023.
[58] W.N. Liu, et al., Life prediction of coated and uncoated metallic interconnect for solid oxide fuel cell applications, J. Power Sources 189 (2) (2009) 1044–1050.
[59] Z. Xu, et al., Mechanical reliability and life prediction of coated metallic interconnects within solid oxide fuel cells, Renew Energy 113 (2017) 1472–1479.
[60] S. Iyer, et al., Review of experimental and modelling investigations for solid oxide electrolysis technology, Int. J. Hydrog. Energy 72 (2024) 537–558.
[61] X. Sun, et al., Durability of solid oxide electrolysis cells for Syngas production, J. Electrochem. Soc. 160 (9) (2013) F1074–F1080.
[62] Y.L. Liu, et al., Microstructure degradation of LSM-YSZ cathode in SOFCs operated at various conditions, Solid State Ion. 206 (2012) 97–103.
[63] C. Graves, et al., Eliminating degradation in solid oxide electrochemical cells by reversible operation, Nat. Mater. 14 (2) (2015) 239–244.
[64] M. Navasa, et al., A three dimensional multiphysics model of a solid oxide electrochemical cell: a tool for understanding degradation, Int. J. Hydrog. Energy 43 (27) (2018) 11913–11931.
[65] M.S. Sohal, et al., Degradation issues in solid oxide cells during high temperature electrolysis, J. Fuel Cell Sci. Technol. 9 (1) (2012).
[66] Y. Xu, B. Chi, Z. Tu, Performance evaluation and uniformity analysis of multi-stack solid oxide electrolysis cell (SOEC) systems under different arrangements, Int. J. Hydrog. Energy 173 (2025) 151339.

[67] E. Demirel, N. Ayas, Thermodynamic modeling of the water-gas shift reaction in supercritical water for hydrogen production, Theor. Found. Chem. Eng. 51 (1) (2017) 76–87.
[68] Z. Wu, et al., A comprehensive review of modeling of solid oxide fuel cells: from large systems to fine electrodes, Chem. Rev. (2025).
[69] P. Moçoteguy, A. Brisse, A review and comprehensive analysis of degradation mechanisms of solid oxide electrolysis cells, Int. J. Hydrog. Energy 38 (36) (2013) 15887–15902.
[70] S.J. McPhail, et al., Addressing planar solid oxide cell degradation mechanisms: a critical review of selected components, Electrochem. Sci. Adv. 2 (5) (2022) e2100024.
[71] A. Faes, et al., Nickel–Zirconia anode degradation and triple phase boundary quantification from microstructural analysis, Fuel Cells 9 (6) (2009) 841–851.
[72] J. Sehested, Sintering of nickel steam-reforming catalysts, J. Catal. 217 (2) (2003) 417–426.
[73] J. Sehested, J.A.P. Gelten, S. Helveg, Sintering of nickel catalysts: effects of time, atmosphere, temperature, nickel-carrier interactions, and dopants, Appl. Catal. A: Gen. 309 (2) (2006) 237–246.
[74] N.V. Giridhar, et al., Optimal operation of solid-oxide electrolysis cells considering long-term chemical degradation, Energy Convers. Manag. 319 (2024) 118950.
[75] M. Nerat, A reduced-complexity model of the solid oxide fuel cell performance degradation due to the nickel agglomeration in the anode, J. Power Sources 466 (2020) 228309.
[76] M.A. Murmura, Modelling high-temperature electrochemical cells: an engineering perspective, ChemElectroChem 11 (1) (2024) e202300313.
[77] M. Hattori, et al., Effect of aging on conductivity of yttria stabilized zirconia, J. Power Sources 126 (1–2) (2004) 23–27.
[78] N. Jiang, D.W. Eric, Structural stability and conductivity of phase-stabilized cubic bismuth oxides, J. Am. Ceram. Soc. 82 (11) (1999) 3057–3064.
[79] N.A. Arifin, et al., Characteristic and challenges of scandia stabilized zirconia as solid oxide fuel cell material – In depth review, Solid State Ion. 399 (2023) 116302.
[80] N. Mahato, et al., Progress in material selection for solid oxide fuel cell technology: a review, Prog. Mater. Sci. 72 (2015) 141–337.
[81] A.S. Farlenkov, et al., Particle coarsening influence on oxygen reduction in LSM–YSZ composite materials, Fuel Cells 15 (1) (2014) 131–139.
[82] M. Palcut, et al., Improved oxidation resistance of ferritic steels with LSM coating for high temperature electrochemical applications, Int. J. Hydrog. Energy 37 (9) (2012) 8087–8094.
[83] D. Larrain, J. Van herle, D. Favrat, Simulation of SOFC stack and repeat elements including interconnect degradation and anode reoxidation risk, J. Power Sources 161 (1) (2006) 392–403.
[84] O. Babaie Rizvandi, X.-Y. Miao, H.L. Frandsen, Multiscale modeling of degradation of full solid oxide fuel cell stacks, Int. J. Hydrog. Energy 46 (54) (2021) 27709–27730.
[85] M. Linder, et al., Model-based prediction of the ohmic resistance of metallic interconnects from oxide scale growth based on scanning electron microscopy, J. Power Sources 272 (2014) 595–605.
[86] Y. Wang, et al., Degradation of solid oxide electrolysis cells: phenomena, mechanisms, and emerging mitigation strategies—a review, J. Mater. Sci. Technol. 55 (2020) 35–55.
[87] M. Keane, et al., LSM–YSZ interactions and anode delamination in solid oxide electrolysis cells, Int. J. Hydrog. Energy 37 (22) (2012) 16776–16785.
[88] C. Graves, et al., Sustainable hydrocarbon fuels by recycling CO2 and H2O with renewable or nuclear energy, Renew. Sustain. Energy Rev. 15 (1) (2011) 1–23.
[89] M. Lang, et al., Electrochemical quality assurance of solid oxide electrolyser (SOEC) stacks, J. Electrochem. Soc. 166 (15) (2019) F1180.
[90] K.J. Yoon, et al., Advances in high-temperature solid oxide electrolysis technology for clean hydrogen and chemical production: materials, cells, stacks, systems and economics, Prog. Mater. Sci. 154 (2025) 101520.
[91] M. Lang, et al., Electrochemical quality assurance of solid oxide electrolyser (SOEC) stacks, J. Electrochem. Soc. 166 (15) (2019) F1180–F1189.
[92] M. Palcut, et al., Corrosion stability of ferritic stainless steels for solid oxide electrolyser cell interconnects, Corros. Sci. 52 (10) (2010) 3309–3320.
[93] G. Cinti, et al., Co-electrolysis of water and CO2in a solid oxide electrolyzer (SOE) stack, Int. J. Energy Res. 40 (2) (2016) 207–215.
[94] J. Sehested, Sintering of nickel steam-reforming catalysts: effects of temperature and steam and hydrogen pressures, J. Catal. 223 (2) (2004) 432–443.
[95] V. Menon, et al., A model-based understanding of solid-oxide electrolysis cells (SOECs) for syngas production by H2O/CO2 co-electrolysis, J. Power Sources 274 (2015) 768–781.
[96] X. Luo, et al., The properties of the fuel electrode of solid oxide cells under simulated seawater electrolysis, Int. J. Hydrog. Energy 48 (28) (2023) 10359–10367.
[97] C.I. Méndez, J. Ancheyta, Modeling of Fischer–Tropsch Synthesis reactor, Math. Model. Complex React. Syst. Oil Gas Ind. (2024) 303–433.
[98] J. Kondoh, et al., Effect of aging on yttria-stabilized zirconia: I. A study of its electrochemical properties, J. Electrochem. Soc. 145 (5) (1998) 1527.